J. Fluid Mech. (1990), *vol.* 219, *pp.* 25–50
Printed in Great Britain

The shape and stability of pinned rotating annular menisci

By P. D. WEIDMAN[1]†, S. KRUMDIECK[2] AND P. ROUSE[2]

[1] School of Mathematics, University of East Anglia, Norwich, NR4 7TJ, UK

[2] Department of Mechanical Engineering, University of Colarado, Boulder, CO 80309, USA

(Received 29 August 1989)

Laboratory measurements on the instability of axisymmetric capillary surfaces pinned to the corners of annular grooves of rectangular section rotating at constant angular velocity Ω have been conducted. In stable configurations the fluid contact lines remain pinned to the corners of the groove with contact angles $\theta_{1,2}$ relative to the inner and outer vertical walls. Using water as the test fluid in narrow grooves of nearly constant width, the critical frequency Ω_c for instability generally decreases with increasing overfill volume ΔV and mean groove radius. Numerical integration of the describing equation gives the shape of the rotating meniscus as a function of five independent parameters. In the range of contact angles $\theta_{1,2} < \pi$, a comparison of experimental results with numerically computed meniscus profiles suggests three mechanisms for contact line movement based on the effective static advancing (θ_A) and receding (θ_R) contact angles for liquid pinned to a sharp corner. Measurements of critical frequencies over a wide range of overfill volumes in six different grooves are in favourable agreement with composite regime diagrams for the critical static meniscus configuration. An interesting feature of this system is the existence of a range of overfill volumes inaccessible to experiments conducted by fixing the overfill volume on a stationary disk and subsequently elevating the disk rotation until contact line movement is observed. Numerical studies showing the effects of Bond number, groove curvature and contact angle hysteresis are presented.

1. Introduction

In this investigation we consider an annular liquid-filled groove formed in the surface of an otherwise horizontal plate executing rigid rotation about the vertical axis of symmetry. The liquid is pinned to the inner and outer corners of the groove and the system is subjected to a uniform gravitational field aligned with the axis of rotation. In question is the shape of the meniscus formed by overfilling the groove and the condition for motion of its contact lines. Meniscus shapes are found by numerical integration of a modified form of the equation of Young and Laplace which takes into account both gravitational and centripetal force fields. Stability is explored experimentally and evidence suggests that for contact angles less than $\frac{1}{2}\pi$, approximately, contact line movement is controlled solely by the intrinsic advancing and receding contact angles of the system. The problem of contact line movement, therefore, is reduced to the problem of calculating the shapes of pinned annular

† Permanent address: Department of Mechanical Engineering, University of Colorado, Boulder, CO 80309, USA.

capillary surfaces in solid-body rotation about their axis of symmetry. It will be seen that even this simple problem gives rise to interesting regime diagrams for incipient contact line movement, owing to the presence of the corners to which the menisci are pinned and also to contact angle hysteresis. No stability analysis of this problem has been attempted. Indeed, one must be careful to distinguish between the existence and the stability of a solution for a rigidly rotating liquid ring. The theoretical aspects of the problem presented here only relate to annular menisci in their 'critical static configuration' (cf. Dussan V. 1985), referring to the condition of incipient contact line movement.

Surprisingly, a review of the literature starting with Finn's (1986) monograph on equilibrium capillary surfaces does not reveal any work on the shape of pinned, rotating axisymmetric menisci formed in finite annular domains subjected to a uniform gravitational field. A considerable number of investigations have dealt with the shape and stability of stationary circular (closed) menisci in a uniform gravitational field; for these the reader is referred to Padday & Pitt (1973), Michael & Williams (1977), Finn (1986) and references cited therein. Somewhat akin to the present problem is the study by Goodwin, Rice & Middleman (1988) on the shape and motion of isolated liquid drops in contact with a horizontal rotating plate. Both this latter study and the present investigation are concerned with the balance of surface tension, gravitational and centripetal forces.

Experiments and analysis of wave motion on the surface of liquid-filled channels with pinned edge conditions have been reported by Scott & Benjamin (1978) and Benjamin & Scott (1979) for straight (two-dimensional) channels and by Heckerman *et al.* (1979) for axisymmetric (three-dimensional) channels. These systems are novel in that the fixed edge conditions impart an additional hydrodynamic cross-channel loading which significantly augments the phase speed of linear progressive waves in narrow channels. While these and additional studies by Benjamin (1980), Benjamin & Graham-Eagle (1985) and Weidman & Norris (1987) all represent analyses of wave motion on pinned static menisci, none have dealt with the problem of contact line stability.

Analyses of contact line stability for two-dimensional static menisci have been reported by Michael & Williams (1977) using a thermostatic approach and Davis (1980) using small-disturbance hydrodynamic theory. In both investigations various boundary conditions related to different material systems were considered. To formulate a tractable problem, Davis (1980) considered the limit of zero Bond number where cross-sectional meniscus profiles take the form of circular arcs intersecting a smooth horizontal plane. For fixed contact lines he found that all wavenumbers are stable for contact angles $\alpha < \frac{1}{2}\pi$ and that wavenumbers greater than $\frac{1}{2}\sqrt{3}$ are stable for contact angles $\alpha < \pi$. Michael & Williams (1977) found that circular sessile drops are stable to axisymmetric disturbances and to the first asymmetric mode for all $\alpha < \pi$. Thus both straight static rivulets of the type considered by Davis (1980) and closed sessile drops are unconditionally stable for all $\alpha < \frac{1}{2}\pi$. Although the present experiments fall into the range $\alpha < \frac{1}{2}\pi$, nothing definitive can be inferred about the stability of the rotating menisci owing to differences in meniscus geometry and the absence of Coriolis forces in the above-cited stability analyses. Furthermore, the above investigations consider liquid wetting a flat horizontal surface whereas the present experiments have been performed for liquid pinned to and overfilling a channel of rectangular section. Also, the results of Davis (1980) do not apply because his models are founded on linear contact angle

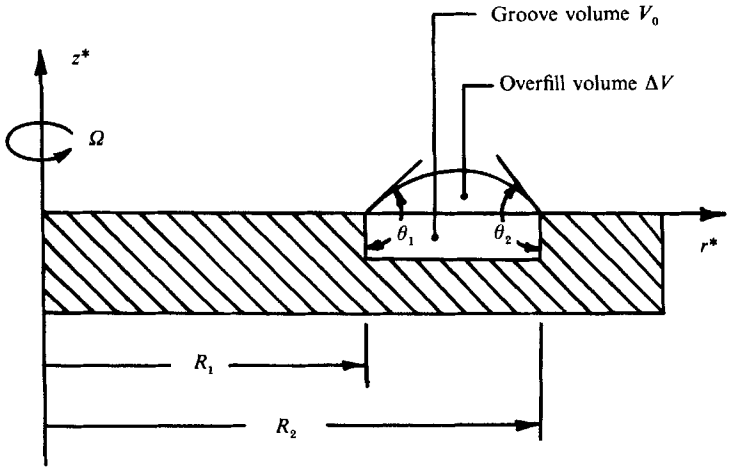

FIGURE 1. Cross-section of circular disk with liquid-filled annular groove.

behaviour, different from the nonlinear condition of contact angle hysteresis of interest in this study.

Formulation of the problem, numerical solution for meniscus profiles and necessary and sufficient conditions for stationary contact lines are presented in §2. The experimental set-up for the measurement of contact line movement described in §3 is followed by a presentation of results in §4. Numerical parameter studies are given in §5 and the paper concludes with a discussion and closing remarks in §6.

2. Problem formulation and numerical solution

A schematic diagram showing a meniscus profile formed by overfilling an annular groove of rectangular section is presented in figure 1. We assume axisymmetric motion and employ cylindrical coordinates (r^*, z^*) for which $\bar{k}$ is the unit vector along the vertical z^*-axis. The inner and outer walls of the channel have radii R_1 and R_2, respectively, and the groove has depth D sufficiently large that a deformed capillary surface never intersects the bottom of the channel. The fluid is subjected to a uniform gravitational field $-g\bar{k}$ and the plate rotates at constant angular velocity $\pm\Omega\bar{k}$. The meridional profile of the axisymmetric meniscus is defined by the equation

$$F(r^*, z^*) = z^* - \zeta^*(r^*) = z^* - [\eta^*(r^*) - \eta_0^*] = 0, \tag{1}$$

where η_0^* is chosen such that $\zeta^*(R_1) = \zeta^*(R_2) = 0$, thus ensuring that the liquid is pinned to the corners of the groove. The local curvature at the free surface is then

$$K(r) = -\nabla \cdot \left(\frac{\nabla F}{|\nabla F|}\right) = -\frac{1}{r^*}\frac{\mathrm{d}}{\mathrm{d}r^*}\left\{r^*\left(\frac{\mathrm{d}\eta^*}{\mathrm{d}r^*}\right)\left[1+\left(\frac{\mathrm{d}\eta^*}{\mathrm{d}r^*}\right)^2\right]^{-\frac{1}{2}}\right\}. \tag{2}$$

The pressure drop across the meniscus is described by the equation of Young and Laplace:

$$p_\ell(r^*) - p_g = -\sigma K(r^*), \tag{3}$$

where p_ℓ and p_g are the liquid and gas pressures adjacent to the free surface, respectively. Both p_g and the surface tension coefficient σ are presumed constant.

For rigid rotation, Euler's equation normal to a streamline gives the pressure in the liquid at the free surface as

$$p_\ell(r^*) - p_0 = \tfrac{1}{2}\rho\Omega^2 r^{*2} - \rho g\eta^*, \tag{4}$$

where p_0 is a constant reference pressure. Inserting (2) and (3) into (4) and non-dimensionalizing r^*, η^* and ζ^* with the channel width $W = R_2 - R_1$ furnishes the boundary-value problem describing the liquid surface profile

$$\frac{\mathrm{d}^2\eta}{\mathrm{d}r^2} = \left[1+\left(\frac{\mathrm{d}\eta}{\mathrm{d}r}\right)^2\right]\left\{\left[Bo\,\eta - \tfrac{1}{2}We\left(\frac{r}{r_1}\right)^2\right]\left[1+\left(\frac{\mathrm{d}\eta}{\mathrm{d}r}\right)^2\right]^{\frac{1}{2}} - \frac{1}{r}\left(\frac{\mathrm{d}\eta}{\mathrm{d}r}\right)\right\}, \tag{5a}$$

$$\frac{\mathrm{d}\eta}{\mathrm{d}r} = \cot\theta_1 \quad \text{at} \quad r = r_1 \equiv \frac{R_1}{W}, \tag{5b}$$

$$\eta(r_1) = \eta(r_2), \tag{5c}$$

in which an arbitrary constant representing a uniform vertical displacement has been omitted. $Bo = \rho g W^2/\sigma$ is the Bond number measuring the relative importance of gravitational to surface tension forces and $We = \rho\Omega^2 R_1^2 W/\sigma$ is a rotational Weber number measuring the relative importance of centripetal to surface tension forces. Zero-Weber-number profiles are described by Padday & Pitt (1973) as gravitationally distorted nodoids or unduloids. Following their classification scheme, profiles at non-zero Bond and Weber numbers for the annular menisci considered here fall into the category of radius-fixed (pinned) nodoids distorted by both gravitational and centripetal acceleration fields. Solutions for the meniscus profiles are governed by five independent parameters: Bo, We, θ_1, r_1 and $\Delta V/V_T$. The normalizing factor $V_T = \pi^2\bar{R}(\frac{1}{2}W)^2$ for the overfill volume, ΔV, is half the volume of a torus of inner radius R_1 and outer radius R_2; thus the torus cross-section is formed by rotating a line of length W in the meridional plane of the liquid ring about its mean radial position $\bar{R} = \frac{1}{2}(R_1+R_2)$. Of course, other choices for the independent non-dimensional parameters are possible.

The inhomogeneous second-order equation for $\eta(r)$ in (5) is nonlinear and admits multiple-valued solutions (see Padday 1971 and Finn 1986 for computed examples at zero Weber number) and hence numerical integrations must be performed with care. In regions where $|\mathrm{d}\eta/\mathrm{d}r|$ becomes large it is convenient to interchange the role of dependent and independent variables. Using the relations

$$\frac{\mathrm{d}r}{\mathrm{d}\eta} = \frac{1}{\mathrm{d}\eta/\mathrm{d}r}, \quad \frac{\mathrm{d}^2r}{\mathrm{d}\eta^2} = -\left(\frac{\mathrm{d}\eta}{\mathrm{d}r}\right)^{-3}\frac{\mathrm{d}^2\eta}{\mathrm{d}r^2}, \tag{6}$$

equation (5) may be rewritten as

$$\frac{\mathrm{d}^2r}{\mathrm{d}\eta^2} = \left[1+\left(\frac{\mathrm{d}r}{\mathrm{d}\eta}\right)^2\right]\left\{\frac{1}{r} - \left[Bo\,\eta - \tfrac{1}{2}We\left(\frac{r}{r_1}\right)^2\right]\left[1+\left(\frac{\mathrm{d}r}{\mathrm{d}\eta}\right)^2\right]^{\frac{1}{2}}\right\}. \tag{7}$$

We have chosen to numerically integrate (5) for $\eta = \eta(r)$ in regions where $|\mathrm{d}\eta/\mathrm{d}r| \leqslant 1$ and switch to integrate (7) for $r = r(\eta)$ in regions where $|\mathrm{d}r/\mathrm{d}\eta| \leqslant 1$. Different parametric forms of the equations have been considered (cf. Princen & Mason 1965; Concus 1968; Huh & Scriven 1969; Padday 1971) to avoid singular behaviour at critical points, but our scheme works quite satisfactorily. A standard shooting technique was employed using a variable-order Adams predictor-corrector IMSL algorithm. For fixed values of Bo, We, θ_1 and r_1, $\eta = \eta_1$ is specified at $r = r_1$ and

Track	R_1 (cm)	W (cm)	D (cm)	T (°F)	H (%)	Bo	r_1
1	0.857	0.372	0.2473	68	87	1.860	2.304
2	2.073	0.383	0.2493	69	81	1.967	5.418
3	3.658	0.373	0.2464	69	85	1.875	9.795
4	6.344	0.388	0.2496	68	85	2.026	16.339
5	8.916	0.382	0.2454	68	92	1.965	23.317
6	11.429	0.366	0.2486	68	92	1.798	31.272
7	13.982	0.384	0.2543	67	88	1.984	36.393

TABLE 1. Annular groove dimensions for the seven tracks and average experimental conditions for measurements conducted in each track

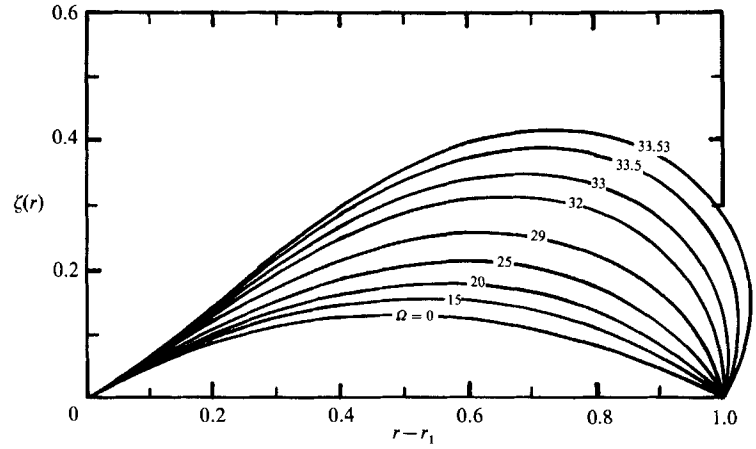

FIGURE 2. A family of capillary surface profiles computed at $Bo = 0.01967$ for Track 2 having inner contact angle $\theta_1 = 120°$.

integration is carried out to $r = r_2$ where η_2 and θ_2 are evaluated; if $\eta_1 \neq \eta_2$ iteration on η_1 proceeds until $\eta_1 = \eta_2 \equiv \eta_0$. The overfill volume under the curve $\zeta(r)$ is also calculated for comparison with experiment. If in addition ΔV is specified, an outer loop iterating on θ_1 is required. A routine for backwards integration was also developed so that θ_2 could be specified in lieu of θ_1.

Experiments to be presented in §4 were conducted in seven concentric grooves of nearly equal width and depth machined in a flat aluminium plate. We henceforth refer to these grooves as Tracks 1–7 and note that their mean radii increase with increasing track number. Measured channel dimensions are given in table 1 along with other pertinent experimental data. We present sample calculations of capillary surface profiles in steady rotation at $Bo = 0.0197$ corresponding to axisymmetric menisci formed in Track 2 with distilled water in a gravitational field 1/100th that of Earth's gravity. Figure 2 shows a family of free-surface profiles all with inner contact angle $\theta_1 = 120°$. Each curve corresponds to a unique combination of Ω and ΔV. Since the radial and vertical coordinates are both normalized with W and plotted on uniform scales, the figure exhibits proportionately correct free-surface profiles. Note that the overfill volume increases with increasing Ω and multiple-valued profiles at the outer rim are observed for $\Omega > 32$ rad/s, approximately. As described in §3, most stability measurements were conducted by metering a prescribed overfill volume ΔV of water into a groove and then increasing Ω until contact line movement

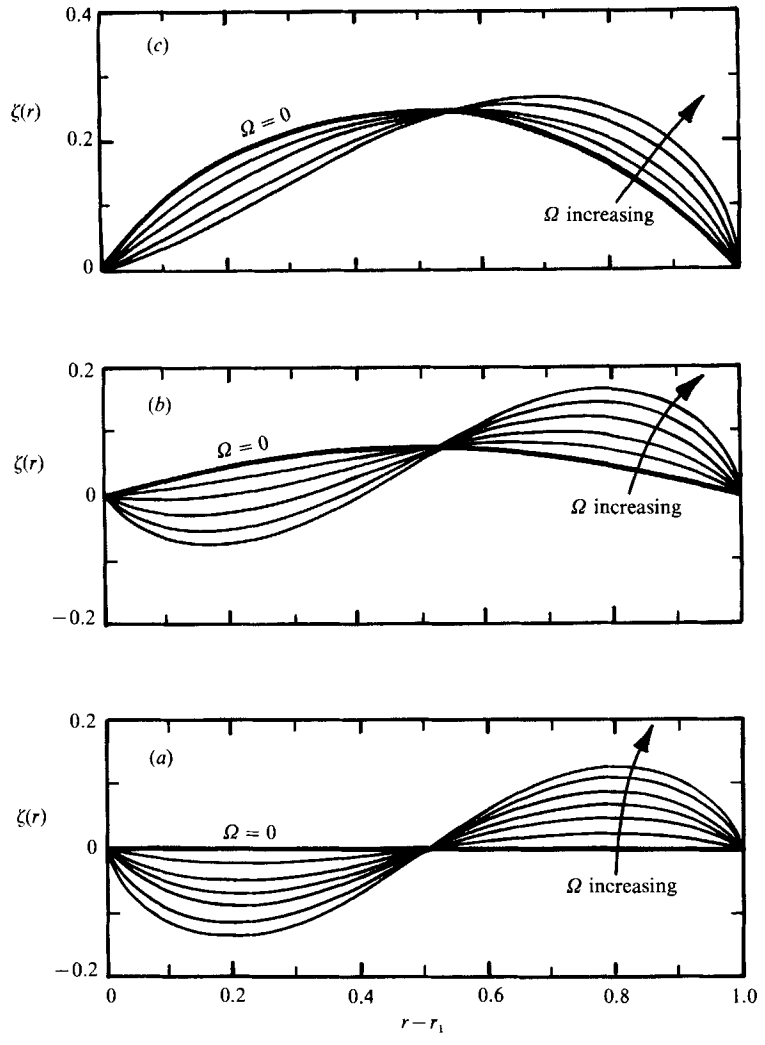

FIGURE 3. Three families of capillary profiles computed at $Bo = 0.01875$ for Track 3 at different overfill volumes: (*a*) $\Delta V = 0$ cm^3; (*b*) $\Delta V = 0.010$ cm^3; (*c*) $\Delta V = 0.035$ cm^3. The thick line profiles correspond zero plate rotation.

was observed. Capillary surfaces corresponding to this type of experiment at $Bo = 0.0188$ in Track 3 are presented in figure 3 for three overfill volumes: (*a*) zero overfill volume corresponding to a flat surface at zero rotation, (*b*) a shallow overfill volume $\Delta V = 0.10$ ml, and (*c*) a large overfill volume $\Delta V = 0.35$ ml. In each figure the profile at zero rotation is marked by a thick line and the evolution of profiles with increasing angular speed is indicated by the direction of the arrows. Note that each set of profiles exhibits a mutual point of intersection that progressively shifts towards the outer rim as the overfill volume increases. Similar profile intersection behaviour for non-rotating menisci in a vertical right circular cylinder may be seen in the calculations presented by Concus (1968). Conditions for movement of a contact line for capillary profiles like those presented in figures 2 and 3 are established in the following section.

2.1. *Condition for incipient contact line movement*

Coghill & Anderson (1923) have performed definitive experiments demonstrating that the static contact angle α of a liquid pinned to a corner with included angle β is free to pivot through the angular range

$$\alpha_R < \alpha < (\pi - \beta) + \alpha_A \tag{8}$$

relative to one of the two intersecting planes forming the corner. For $\beta = \pi$ when the corner degenerates to a flat surface, one recovers the usual relation for contact angle hysteresis where the contact line remains stationary for values of α between the receding contact angle α_R and the advancing contact angle α_A. The contact angle hysteresis $(\alpha_A - \alpha_R)$ in certain liquid–solid systems can be quite large. For example, Dettre & Johnson (1965) report contact angle hysteresis of nearly 90° for water on titanium-coated glass after treatment with a sodium stearate solution and a number of coating treatments with polydibutyl titanate. In the present experiments $\beta = \frac{1}{2}\pi$. Thus, according to (8) contact angle variability at the inner and outer corners of each groove is increased by $\frac{1}{2}\pi$ over and above the natural contact angle hysteresis of the system. In terms of θ defined relative to the vertical channel walls (cf. figure 1) the static contact angles may assume any value in the range

$$\alpha_R < \theta_{1,2} < \tfrac{1}{2}\pi + \alpha_A. \tag{9}$$

Equation (9) represents the necessary and sufficient conditions for the existence of a static contact line at a corner of included angle $\frac{1}{2}\pi$, and hence the corresponding profiles for pinned static menisci are represented by solutions of (5) satisfying (9).

We now investigate different possibilities for contact line movement according to (9). Consider first the case of a stationary plate for which $\Omega = 0$. Numerical solutions show that, owing to the compound curvature of the system, $\theta_1 > \theta_2$ for all positive overfill volumes. Thus, as the liquid volume supported by the channel increases, an overfill volume $(\Delta V)_0$ is reached for which $\theta_1 = (\theta_1)_A \equiv \frac{1}{2}\pi + \alpha_A$ and the contact line can no longer remain at the inner rim. In this case the fluid initially must move radially inward across the interior horizontal surface in the direction of the arrow in figure 4(*a*). Contact line movement by this mechanism is expected to occur at high overfill volume and low angular speed.

Now consider what happens when the plate begins to rotate. As shown in figure 3, the centre of gravity of the overfill volume gradually shifts towards the outer rim and a speed is reached beyond which $\theta_2 > \theta_1$. As Ω increases, the contact angle at the outer rim will ultimately attain the value $\theta_2 = (\theta_2)_A \equiv \frac{1}{2}\pi + \alpha_A$ whence the contact line can no longer be maintained there. In this case the liquid initially must move radially outward across the exterior horizontal surface in the direction of the arrow in figure 4(*b*). For example, consider water at 0.01 times Earth's gravity filling Track 2 with an advancing contact angle $\alpha_A = 84°$. Figure 5 displays a family of free-surface profiles spanning that channel for $\theta_2 = (\theta_2)_A = 174°$ corresponding to the condition for incipient contact line movement at the outer rim. Not shown are profiles for $\Omega < 10$ rad/s for which $\theta_1 > \theta_2$. Above this critical frequency $\theta_2 > \theta_1$, and the contact line at the outer rim is prone to move at sufficiently high rotational speed. Note that, in contrast to the results presented in figure 2, the overfill volume decreases with increasing Ω. This is in accordance with intuition since small overfill volumes are substantially more difficult to centrifuge out of the rotating groove than large volumes. (We differentiate between $(\theta_1)_A$ and $(\theta_2)_A$ since if the inner and outer corners of a groove were constructed using different materials, the advancing contact angles

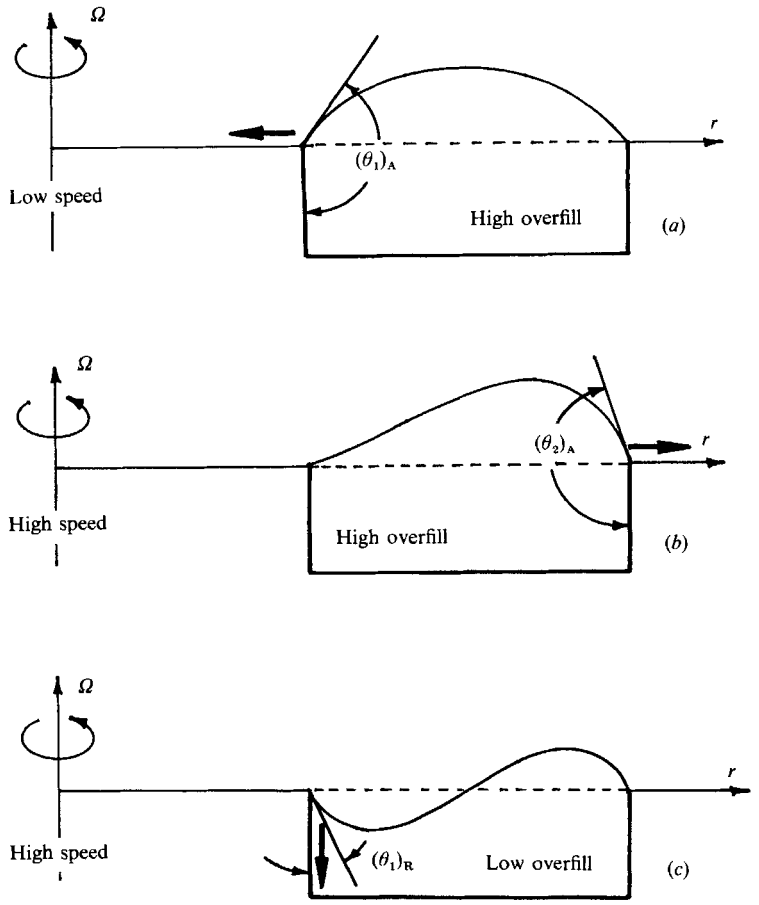

FIGURE 4. Diagram showing the three limiting contact angles which give rise to contact line movement in the direction indicated by the arrows. The criteria are: (*a*) $\theta_1 \geqslant (\theta_1)_A$ with incipient motion to the left; (*b*) $\theta_2 \geqslant (\theta_2)_A$ with incipient motion to the right; and (*c*) $\theta_1 \leqslant (\theta_1)_R$ with incipient motion down the inner wall.

at each corner would be independent parameters of the system.) Contact line movement by this mechanism is expected to occur at moderate-to-high overfill volume and moderate-to-high angular speed.

Another possibility exists for (5) and (9) not to be satisfied. Referring to figure 1, the fluid always advances clockwise around the outer corner, either by an increase in overfill volume or an increase in plate angular speed. The fluid may either advance counterclockwise around the inner corner if liquid is added to the groove, or recede clockwise around it if the rotation frequency increases. It is this latter condition that gives rise to a third mechanism for contact line movement. Suppose in the example of figure 5 that $\alpha_R = 60°$. Then for rotation rates greater than 45 rad/s, approximately, the condition $\theta_1 = (\theta_1)_R \equiv \alpha_R$ is reached before $\theta_2 = (\theta_2)_A = 174°$ indicating that the contact line at the inner rim must move. In this case the fluid initially must recede down the inner vertical wall in the direction of the arrow in figure 4(*c*). This mechanism for incipient contact line motion is expected to be relevant at low overfill volume and high angular speed.

We are now in a position to construct a composite regime diagram for incipient

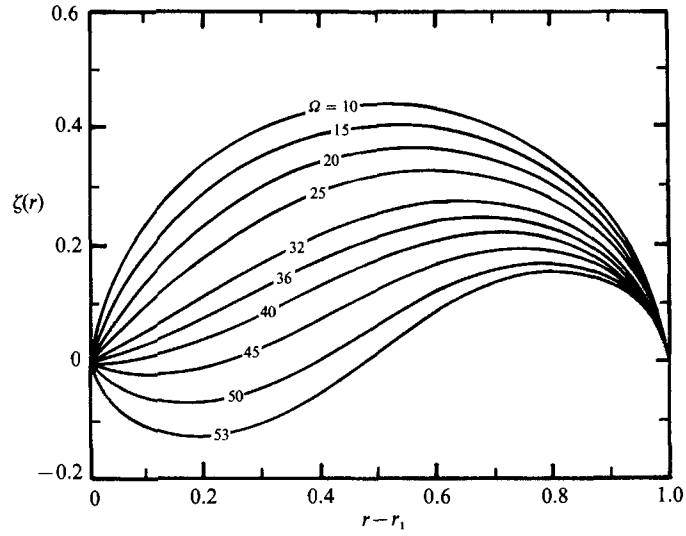

FIGURE 5. A family of free-surface profiles computed at $Bo = 0.01967$ for Track 2 having outer contact angle $\theta_2 = 174°$.

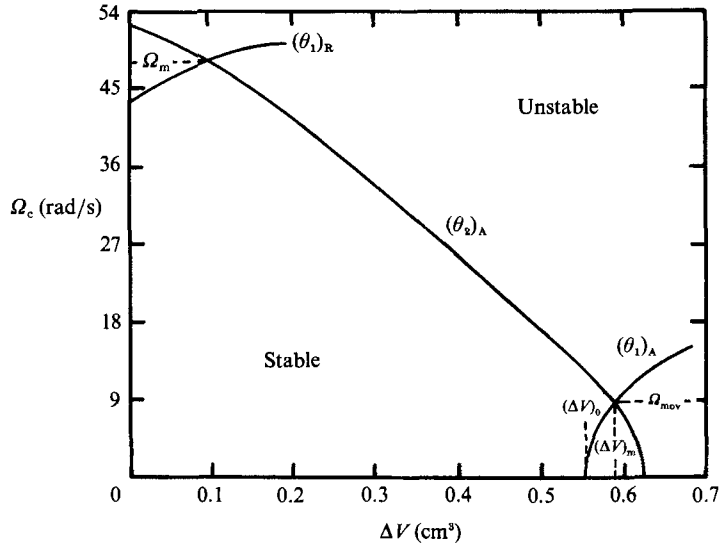

FIGURE 6. Composite stability boundary at $Bo = 0.01967$ for Track 2. The curves marked $(\theta_1)_R$ and $(\theta_{1,2})_A$ correspond to stability branches computed for $(\theta_1)_R = 45°$ and $(\theta_{1,2})_A = 165°$, respectively.

contact line movement based on the three mechanisms described above. To fix ideas, we take $Bo = 0.0197$, $r_1 = 2.073$, $\alpha_R = 45°$ and $\alpha_A = 75°$. We define Ω_c as the critical angular rotation rate for which either contact line becomes dislodged from its rim at overfill volume ΔV. The boundaries for the critical static configuration in $(\Omega_c, \Delta V)$-space are presented in figure 6. At small rotation rates, the domain is bounded by the curve labelled $(\theta_1)_A$ and movement first occurs as an inward displacement of the inner contact circle when $\theta_1 = (\theta_1)_A = 165°$. At small overfill volumes, the domain is bounded by the curve labelled $(\theta_1)_R$ and motion first occurs as a downward displacement of the inner contact circle when $\theta_1 = (\theta_1)_R = 45°$. These two boundaries

are intersected by the curve labelled $(\theta_2)_A$ and here movement first occurs as an outward displacement of the contact circle at the outer rim when $\theta_2 = (\theta_2)_A = 165°$.

Several aspects of the regime diagram in figure 6 may now be interpreted with regard to a physical experiment. Perhaps the most interesting feature is the existence of a small domain corresponding to overfill volumes $(\Delta V)_0 \leqslant \Delta V \leqslant (\Delta V)_m$ which can be accessed only by adding liquid to the groove while it is rotating. The maximum overfill volume $(\Delta V)_m$ is that corresponding to the solution for which $(\theta_1)_A = (\theta_2)_A$. The rotation speed at this point of maximum overfill volume is denoted Ω_{mov}. For $0 \leqslant (\Delta V) < (\Delta V)_0$ the experiment may be carried out by the simple expedient of filling the groove of a stationary disk and then increasing the angular speed until contact line movement is first observed. At low overfill volumes there exists a maximum rate of angular rotation Ω_m defined by the solution for which $(\theta_1)_R = (\theta_2)_A$. Finally, one may observe that both the $(\theta_1)_A$ and $(\theta_2)_A$ boundaries perpendicularly intersect the ΔV-axis, a condition which might have been anticipated considering the invariance of equation (5) with respect to the sign of Ω. An experiment designed to test the above mechanisms for incipient contact line movement is described in the following section.

3. The experiment

3.1. *Apparatus*

A rotating table was constructed to investigate the stability of pinned axisymmetric menisci rotating at constant angular velocity. The stationary frame consisted of two thick horizontal aluminium plates bolted together with machined spacer tubes and was supported underneath by three adjustable, shock-mounted aluminium legs attached to a concrete floor. The spindle assembly, housing two thrust bearings and the rotating shaft, was mounted vertically through the vertically separated horizontal plates. A cylindrical flange mounted at the top end of the rotating shaft contained a bolt circle for attaching the circular test plate. The rotating shaft was driven by a $\frac{1}{2}$ HP stepper motor via a belt-and-pulley system. Included in the drive chain was a large (Volkswagen) flywheel to minimize sudden changes in angular acceleration. The system was equipped with a light beam encoder interrupted by 150 equally spaced holes located around a circle on a thin disk concentric to and rotating with the drive shaft. The average period measured by a timer-counter for the passage of 10 or 100 holes past the encoder was used to determine the angular velocity of the plate. The stepper motor was controlled by a Superior Electric indexer providing two continuously adjustable speed ranges. Accessible disk speeds fell in the range $3 \leqslant \Omega \leqslant 100$ rad/s, the lower limit set by cogging of the stepper motor under the high inertia of the system.

The test plate with seven concentric grooves of nearly equal rectangular section was machined from 6061-T6 aluminium stock with final groove dimensions as listed in table 1. The grooves had an average width $\overline{W} = 0.378$ cm, but width variations of as much as 5% existed from track to track. The top corners of each groove were rounded to a radius of 0.15 mm, approximately. After machining, the plate was hard anodized and all surfaces except the bottom of each groove were polished smooth to a roughness of 0.5 μm. Since the interesting aspects of this experiment are contact-angle dependent, the plate was not pretreated with a hydrophilic polymer solution. With the disk bolted in place the runout at its outer edge measured ± 0.02 mm, showing excellent concentricity with the drive shaft. Levelling the support frame

gave a maximum inclination of 0.12° for the test plate throughout a complete rotation as measured by a calibrated level spirit.

Loss of water from a groove, due in part to evaporation in the dry climate of Colorado where the experiments were performed and in part to forced convection set up by the relative motion between air and the rotating liquid surface, was a particular concern. Forced convection evaporation was minimized by placing a transparent Plexiglas cover over the test plate after filling a groove with liquid. The cover fitted snugly around the outer rim thereby sealing air in the 15 mm gap above the surface of the plate. Natural evaporation was retarded by performing the experiments at elevated humidity in a control chamber. As shown in table 1 all experiments were conducted at relative humidities in the range 81–92% and at temperatures near 68 °F. A description of the control chamber is given in the Appendix along with measurements of the evaporation rate of water under experimental conditions and an analysis of errors. We find that errors due to water evaporation, accuracy in reading pipette volumes and accuracy in measuring angular velocities all fall within the diameter of a plotting symbol for measurements presented in figures 7 and 8. The error bars for these data measure the *repeatability* of critical frequency or overfill volume at which first contact line movement was observed by the naked eye for experiments performed under nearly identical ambient conditions.

In spite of the fact that the stepper motor was shock-mounted to the concrete floor and separated from the rotating table, very weak high-frequency vibrations transmitted through the floor and/or the belt-and-pulley system to the support platform could be discerned. Although it can be expected that above a certain threshold external vibrations will cause premature instability, the quantitative effect of the table's acceleration noise on the stability measurements is difficult to assess. The r.m.s. amplitude variation of this 'g-jitter' as a function of disk frequency was measured and is presented in the Appendix. The maximum r.m.s. g-jitter recorded was less than 0.2% of Earth's gravity.

3.2. *Measurement procedure*

The experimental procedure for determining the critical frequency Ω_c of contact line movement at fixed overfill volume is described below. Ambient conditions in the test chamber were set near 68 °F in the neighbourhood of 85–90% relative humidity. The test fluid employed in all experiments was high-performance liquid chromatography (HPLC) grade water. Before an experiment the test groove was cleaned with ethyl alcohol and rinsed two or three times with HPLC grade water. Water from the last rinse was absorbed with lint-free tissue and final drying took place via natural evaporation. A 5 ml pipette readable to ± 0.005 ml was used to meter water into Tracks 1–3 and a 10 ml pipette accurate to ± 0.025 ml (or a combination of these pipettes) was used for Tracks 4–7. Prior to each experiment the groove was inspected to ensure that the water made smooth contact around both rims of the channel, a procedure particularly important at low overfill volumes to ascertain that the liquid was uniformly pinned to the inner and outer corners of a groove. Then the Plexiglas cover was mounted and plate rotation initiated. Having located the approximate angular speed for instability in an earlier run, the disk was brought rapidly up to a rotation rate slightly below the expected critical speed. An estimate for the fluid spin-up time is given by the time $\tau = (\frac{1}{2}W)^2/\nu$ for viscous diffusion from the vertical sidewalls. This estimate is considered conservative because it does not include viscous diffusion from the larger bottom surface and excludes any minor contribution

from Ekman pumping. Using $\nu = 0.01$ cm^2/s for water at room temperature gives $\tau \approx 3.6$ s. Based on this estimate the slightly subcritical rotation speed was maintained for a period of approximately 30 s to establish nearly rigid rotation of the liquid in the groove. Subsequently, the speed was gradually increased until contact line movement was observed at which time a trigger signal was sent to the timer-counter to freeze the digital LED display of measured period. Proper illumination of the rotating rivulet through the Plexiglas cover was imperative to minimize reflection and clearly detect first contact line movement. Unfortunately, the corner of the Plexiglas cover interfered with the illumination on the outermost groove and reliable stability measurements for Track 7 could not be made.

The maximum overfill volume that can be supported by a non-rotating groove as noted in figure 6 is $(\Delta V)_0$. The determination of this volume for each channel was made by continuously metering liquid into a stationary groove until contact line movement was observed. These experiments were sensitive to pipette stream disturbances near the onset of instability and to the precision with which the plate was levelled, particularly for the outer grooves. To rectify the latter problem, the test plate was removed from the rotating table, placed on an aluminium platform and levelled to $\pm 0.02°$ with the aid of three fine levelling screws. Concerning the former problem, disturbances produced by water emanating from the pipette were least when the pipette formed a fine narrow stream. At low head large drops formed at the tip of the pipette; since these drops caused a significant ripple while penetrating the liquid surface, this condition was always avoided. At sufficiently low rotation speeds critical overfill volumes fall in the range $(\Delta V)_0 < (\Delta V) < (\Delta V)_m$. At least one data point in this region of the regime diagram for each of the six inner tracks was obtained by continuously overfilling a test groove on the disk rotating at constant Ω until contact line movement was observed.

Measurement of the surface tension coefficient and the apparent (macroscopic) advancing and receding contact angles were made in the test chamber under the average conditions of the experiments, namely at 68 °F and 87 % relative humidity. For a discussion of actual versus apparent contact angles, the reader is referred to the review article by Dussan V. (1979). The surface tension coefficient measured with a Du Nouy tensiometer was $\sigma = 72.8$ dynes/cm. The limiting contact angles were determined by observing the angles at which the contact circle of a spherical liquid drop formed on the surface of the disk would advance or recede. The experiment was carried out by slowly injecting (for measurement of α_A) or withdrawing (for measurement of α_R) HPLC grade water through a small hole drilled normal to the polished aluminium oxide surface midway between Tracks 6 and 7 with the plate levelled to $\pm 0.02°$ by the stationary levelling platform. Direct observations of the advancing and receding contact angles were made with a goniometer focused tangent to the contact circle while sighting at a slight angle ($\approx 2°$) down from horizontal. The goniometer was fabricated in-house by mounting a small microscope with cross-hairs onto the rotational axis of a Melles-Griot goniometer base rotatable through $\pm 45°$ with a vernier scale accurate to 5′ angular displacement. Repeated measurements gave $\alpha_A = 86.5 \pm 1.5°$ and $\alpha_R = 16 \pm 2.0°$. Using a Par Mettler densitometer, the density of HPLC grade water was determined to be $\rho = 0.998$ g/cm^3 and the gravitational constant at the site of the experiments was $g = 979.6$ cm/s^2. This gives an average Bond number for the experiments of $Bo = 1.924$ with ± 6 % variations due to individual differences in the width of each track.

Two comments of particular importance for experiments of the present type are now given. First, application of the sensitive 'shaking test' (Scott 1979) for surface

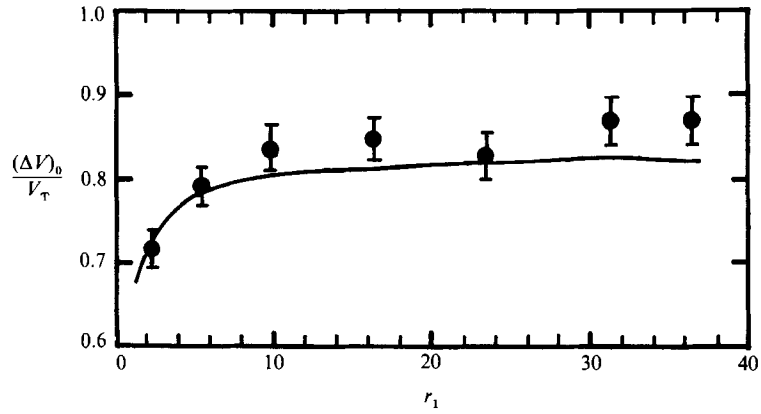

FIGURE 7. Measured maximum overfill volumes at zero rotation as a function of groove curvature. The continuous curve is composed of points computed for the experimental Bond numbers listed in table 1 for each track and additional points computed for the average Bond number $Bo = 1.924$ at other r_1 values. Error bars indicate measurement repeatability.

contamination showed that all bubbles burst upon reaching the free surface in less than 0.5 s for HPLC grade water from a newly opened bottle, but this increased to approximately 1 s with continued use from the same bottle. Kitchener (1964) notes that persistence of bubbles at a water surface for longer than 1 s is indicative of the presence of surface-active impurities. Scott (1981) found, in a double distillation process to prepare surface-clean water for sensitive experiments on capillary–gravity waves, that all surface bubbles ruptured in less than 0.5 s. By comparison, we accepted bottled HPLC water as being sufficiently surface-clean for these preliminary experiments. Second, in spite of a concerted effort to produce a test plate with smooth clean surfaces and uniformly rounded corners, close inspection revealed that the contact lines were not in perfect circular contact around the corners of the grooves. Rather, when viewed under a microscope with 20× magnification, the liquid in the immediate vicinity of the contact line appeared minutely wrinkled around its entire circumference, with the irregular fluid surface smoothing out rapidly away from the irregular line of contact. This feature was observed only on a microscopic scale, however, and to the naked eye the pinned menisci in each groove appeared truly axisymmetric.

4. Experimental results

Experiments to determine incipient contact line movement at nearly constant Bond number (cf. table 1) were made over the following range of non-dimensional parameters: $2.30 \leqslant r_1 \leqslant 36.4$; $0 \leqslant We \leqslant 19.2$; $0 \leqslant \Delta V/V_T \leqslant 0.87$. Measurements of $(\Delta V)_0/V_T$ for the seven tracks are presented in figure 7. The solid line is based on the measured advancing contact angle $(\theta_1)_A = 176.5°$ and was computed for the values of Bo and r_1 listed in table 1 with additional points at other values of r_1 computed at $Bo = 1.924$, the average Bond number for the experiments. The slight waviness in the computed curve is a manifestation of the $\pm 6\%$ Bond-number variation. Unity ordinate in this figure corresponds to the normalized overfill volume at zero Bond number with contact angles $\theta_{1,2} = 180°$ in the asymptotic limit $r_1 \to \infty$ corresponding to straight (two-dimensional) menisci. In the present computations the asymptotic value for the normalized overfill volume (≈ 0.83) is less than unity, owing to the fact

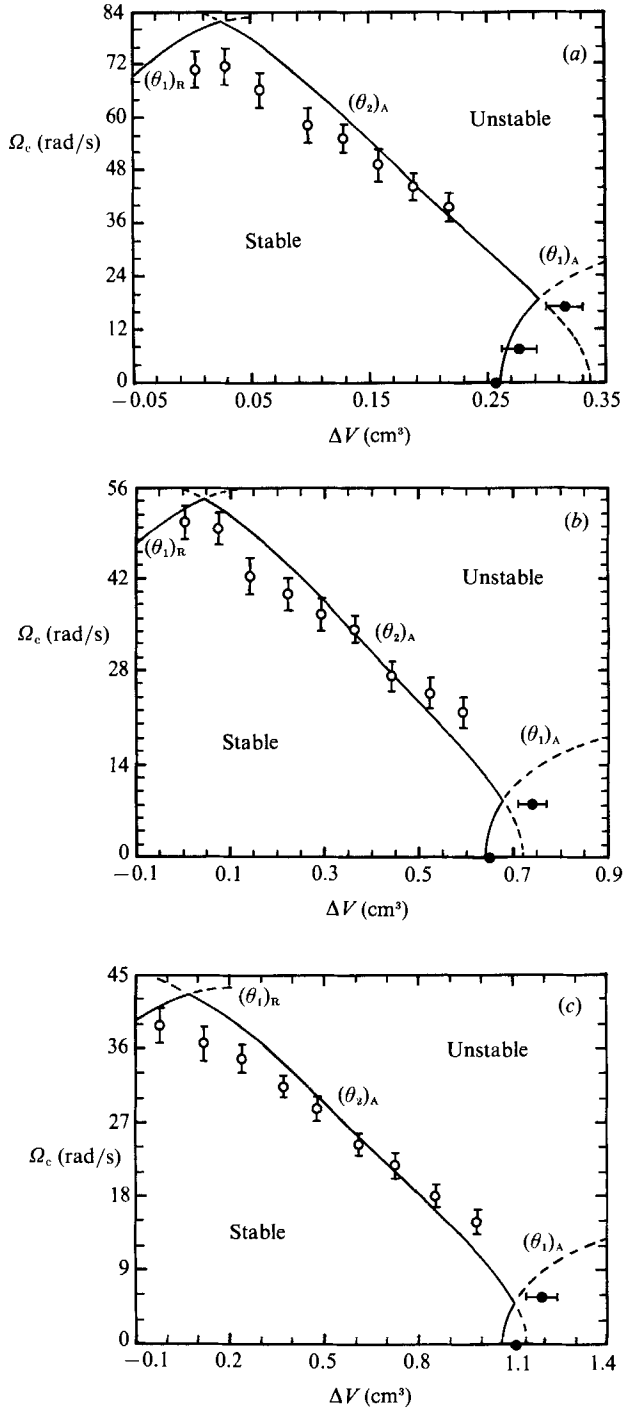

FIGURE 8(*a–c*). For caption see facing page.

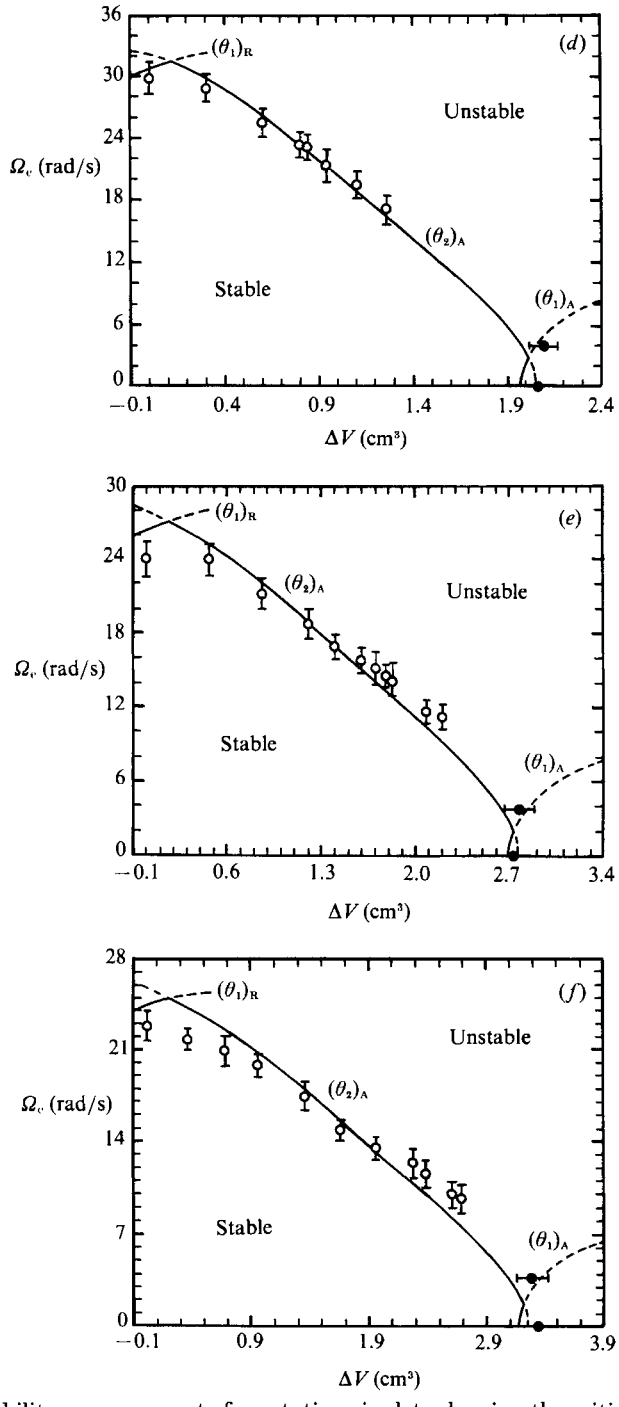

FIGURE 8. Stability measurements for rotating rivulets showing the critical angular speed Ω_c as a function of overfill volume ΔV for: (*a*) Track 1; (*b*) Track 2; (*c*) Track 3; (*d*) Track 4; (*e*) Track 5; and (*f*) Track 6. Open symbols correspond to experiments performed at constant overfill volume and closed symbols correspond to experiments performed at constant angular velocity. Error bars indicate measurement repeatability. The curves labelled $(\theta_1)_R$ and $(\theta_{1,2})_A$ are the solution branches computed at the experimental conditions listed in table 1 for the measured contact angles $(\theta_1)_R = 16°$ and $(\theta_{1,2})_A = 176.5°$, respectively.

that the contact angles were less than 180° and also because the Bond number was not sufficiently small for gravitational effects to be neglected. The r.m.s. error between experiment and theory for the data in figure 7 is 3.8%.

Experimental data for contact line movement of rotating menisci formed in the first six tracks are presented in figure 8. These results are given in dimensional (Ω_c, ΔV)-space to facilitate reference to corner points defined on the regime diagram in figure 6, and also to emphasize the wide range of disk angular frequency and overfill volume covered by the experiments. Open symbols represent experiments conducted at a preset overfill volume and solid symbols represent those conducted at a preset disk rotation rate. The region contained inside the continuous solid boundary represents the domain for which the contact lines are stationary in the rotating frame computed for the conditions of the experiments. Measurements bear out the general trends of the numerically computed boundary for the critical static configuration. For example, data along the primary branch $(\theta_2)_A$ show that the critical angular rotation rate decreases with increasing overfill volume. Also, values of Ω_c near zero overfill volume do not continue to rise following the $(\theta_2)_A$ branch, but remain within the stable bound of the $(\theta_1)_R$ boundary. Furthermore, the existence of a range of overfill volumes $(\Delta V)_0 \leqslant \Delta V \leqslant (\Delta V)_m$ accessible only by adding liquid to a rotating disk is verified. On the one hand, stability measurements performed at fixed overfill volume set slightly below $(\Delta V)_0$ all fall near the upper $(\theta_2)_A$ branch. Experiments conducted at fixed Ω near the $(\theta_1)_A$ branch in figure 8 (*a–c*), on the other hand, always gave critical overfill volumes larger than $(\Delta V)_0$. The fact that overfill volumes measured near Ω_{mov} were larger than the numerically determined values of $(\Delta V)_m$ for each groove can be explained as follows. At the computed corner point $[\Omega_{mov}, (\Delta V)_m]$ the meniscus did not experience contact line movement. Increasing ΔV to a value slightly greater than $(\Delta V)_m$ resulted in a very small displacement in either the inner or outer contact line. In the four or five repeat experiments for Tracks 1–3 performed very near the critical point, overfill volumes larger than $(\Delta V)_m$ were always recorded, probably owing to difficulty in detecting the first subtle movement of a contact line.

There is an unmistakable trend in the experimental data along branches $(\theta_1)_R$ and $(\theta_2)_A$ that is not consistent with the numerically computed regime boundaries. At high rotation rates the measured values of Ω_c always fall below the numerical curves while at low rotation rates the data sometimes lie above the $(\theta_2)_A$ branch. The observation of premature instability at elevated rotation rates is most likely due to the weak high-frequency vibrations of the experimental platform induced by the stepper motor and drive system. Notice in figure 8 that the discrepancy between experiment and computation near Ω_m increases uniformly (within experimental error) with Ω_m, i.e. the 3 rad/s discrepancy at $\Omega_m \approx 25$ rad/s in figure 8 (*f*) rises to about 10 rad/s at $\Omega_m \approx 83$ rad/s in figure 8 (*a*). Ignoring the two small resonances at 20 and 40 rad/s, the r.m.s. acceleration disturbance field measured in figure 15 in the Appendix increases in like manner from about $0.0008g$ to nearly $0.002g$ over the corresponding range of Ω_m, supporting the contention that the observation of premature instability is due to this external disturbance. In figures 8 (*b, c*) and 8 (*e, f*) the measured data along the lower portion of the numerically computed $(\theta_2)_A$ branch fall slightly above that boundary in the unstable region. As pointed out by two referees of this paper, one should expect that the limiting contact angles of water on the anodized surface will vary to some extent across the plate. Thus the measurements of α_A and α_R at the single location between Tracks 6 and 7 may not be indicative of the local advancing and receding contact angles at the rim of each

groove. A variation of the average limiting contact angles from rim to rim could account, at least in part, for the fact that the experiments and theory do not agree to within experimental error.

Apart from the generally favourable agreement between experiment and computation, observations of the instability process were consistent with the proposed mechanisms for contact line movement. Instabilities at zero rotation on the $(\theta_1)_A$ branch appeared as a radially *inward* displacement of the inner contact line with the outer contact circle still pinned, as did the instability observed at $\Omega_c \approx 8$ rad/s along that branch in figure 8(*a*). Near Ω_{mov} contact line motion across either the inner or outer rim was observed. However, owing to weak asymmetries in the experimental set-up and especially in the method of adding liquid to the groove for experiments conducted at fixed angular speed, these instabilities never occurred in an axisymmetric fashion. The menisci remained pinned over most of a groove's circumference with only a *local* displacement of fluid across a corner, typically encompassing 5° arclength for Track 7 and increasing to 30° arclength for Track 1. Thus the first contact line movement evidently occurs at the weakest point of contact around the rim. Contact line movement at high rotational frequencies near the $(\theta_1)_R$ and $(\theta_2)_A$ branches always produced a spontaneous *outward* radial spray of liquid from the grooves. These apparently correspond to a real hydrodynamic instability and can be unambiguously classified as 'explosive', the process being more violent at higher critical rotation speeds, larger mean radii and lower overfill volumes. It might be anticipated that contact line movement near the $(\theta_1)_R$ branch would not be explosive, but rather one whose postcritical state consists of steady rotation at a slightly supercritical speed with only a small displacement of the contact circle down the inner wall. This was not observed, however, apparently because the downward motion of the inner contact line sends a radially propagating disturbance across the meniscus which, upon reaching the opposite rim, momentarily increases the outer contact angle above $(\theta_2)_A$, thus inducing contact line movement there as well.

5. Numerical parameter studies

In the experiment contact line movement for annular axisymmetric rotating menisci is governed by six independent dimensionless variables, Bo, We, $\Delta V/V_T$, θ_A, θ_R and r_1 for circular grooves of rectangular section with included angles $\beta = \frac{1}{2}\pi$ at each corner. (For axisymmetric grooves of varying geometrical section with corners constructed of different solid materials, contact line movement would be governed by a total of nine parameters with θ_A replaced by $(\theta_1)_A$ and $(\theta_2)_A$ and the two remaining parameters being β_1 and β_2, the included angles at the inner and outer corners, respectively.) Therefore, the regime diagram in non-dimensional $(We^{\frac{1}{2}}, \Delta V/V_T)$-space depends on the four remaining parameters, Bo, θ_A, θ_R and r_1. (The square-root of the rotational Weber number is best-suited for displaying the $(\theta_1)_A$ and $(\theta_1)_R$ boundaries.) Since the Bond number was nearly constant for the computations presented in dimensional form in figure 8, only the parameter r_1 was varied substantially. When these results are plotted as $We^{\frac{1}{2}}$ versus $\Delta V/V_T$, it is found that the $(\theta_1)_A$ branch is relatively insensitive to variations in r_1 for the conditions of the experiments. The $(\theta_2)_A$ and $(\theta_1)_R$ branches, on the other hand, are strongly affected as is evident in figure 8 by the substantial rise in Ω_m with decreasing values of r_1; non-dimensionally, the maximum Weber number rises from $We_m^{\frac{1}{2}} \approx 5$ at $r_1 = 36.4$ to $We_m^{\frac{1}{2}} \approx 19$ at $r_1 =$

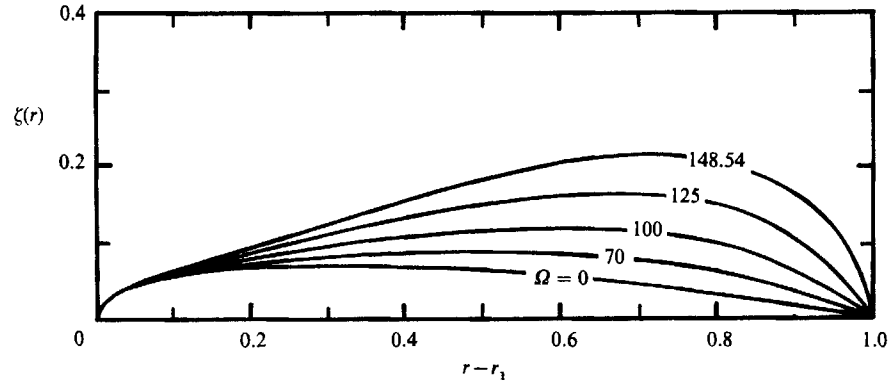

FIGURE 9. Free-surface profiles along the $(\theta_1)_A = 176.5°$ stability branch connecting $(\Delta V)_0$ at zero angular velocity to $(\Delta V)_m$ at $\Omega_{mov} = 148.54$ rad/s computed at the average experimental values $Bo = 1.924$ and $\overline{W} = 0.378$.

2.3. Thus, in the range of r_1 values explored, decreasing r_1 at fixed width W enhances the stability of pinned rotating menisci primarily through a stabilization of the $(\theta_2)_A$ and $(\theta_1)_R$ domain boundaries.

We conclude this investigation by presenting three additional parameter studies. In the first study the region of 'inaccessible' overfill volumes governed by the $(\theta_1)_A$ domain boundary is considered in detail over a wide range of r_1. The second study elucidates the effect of Bond number on the stability diagram and the final study exhibits the influence of contact angle hysteresis.

5.1. *Maximum overfill volume*

Examination of the results in figure 8 shows that $(\Delta V)_m/(\Delta V)_0$ increases with decreasing values of r_1 and the range of inaccessible static states for experiments conducted at preset overfill volumes can be significant. Consider, for example, the family of $(\theta_1)_R$ profiles in figure 9 computed at the average Bond number for the laboratory experiments, but with inner radius $R_1 = 0.01$ cm. Integration gives $(\Delta V)_0 = 0.00791$ cm^3 and $(\Delta V)_m = 0.0299$ cm^3 at $\Omega_{mov} = 148.5$ rad/s. Thus nearly 75% of the overfill volumes can only be accessed by adding liquid to the rotating groove for this small parameter value, $r_1 = 0.0265$.

Numerical computations at the average conditions of the experiments, $Bo = 1.924$ and $\overline{W} = 0.378$ cm, have been conducted to investigate the dependence of $(\Delta V)_m$, $(\Delta V)_0$ and Ω_{mov} on r_1. The results of this parameter study are presented in log–log form in figure 10. For $r_1 \gg 1$ numerical results yield the following approximate asymptotic behaviours:

$$\left.\begin{aligned} (\Delta V)_m &\sim 17.5 r_1 \quad (\text{cm}^3), \\ \Omega_{mov} &\sim \frac{25}{r_1} (\text{rad/s}) \\ \frac{(\Delta V)_m}{(\Delta V)_0} &\sim 1. \end{aligned}\right\} \quad (r_1 \to \infty), \tag{10a, b, c}$$

The limiting forms in (10*b*) and (10*c*) for $r_1 \to \infty$ are consistent with the two-dimensional configuration to which they correspond, namely $(\Delta V)_0$ is the maximum overfill volume which must occur at zero angular velocity. The fact that both $(\Delta V)_0$

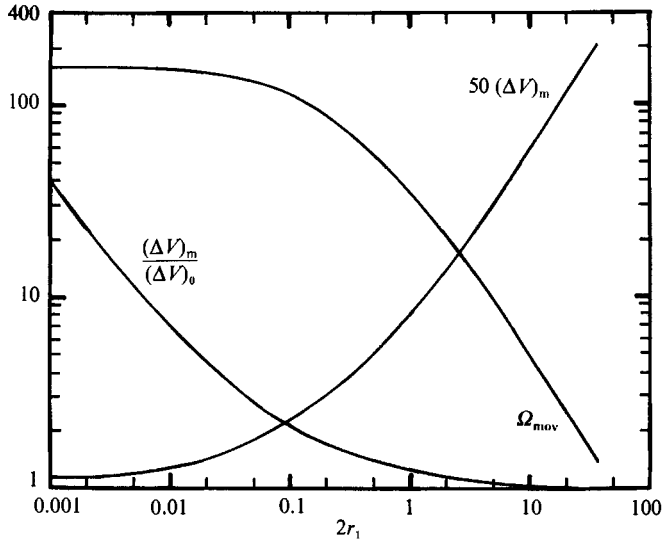

FIGURE 10. Variations of the maximum overfill volume $(\Delta V)_m$, its ratio to $(\Delta V)_0$ and its corresponding angular speed Ω_{mov} as a function of r_1 computed at the average experimental values $Bo = 1.924$ and $\overline{W} = 0.378$.

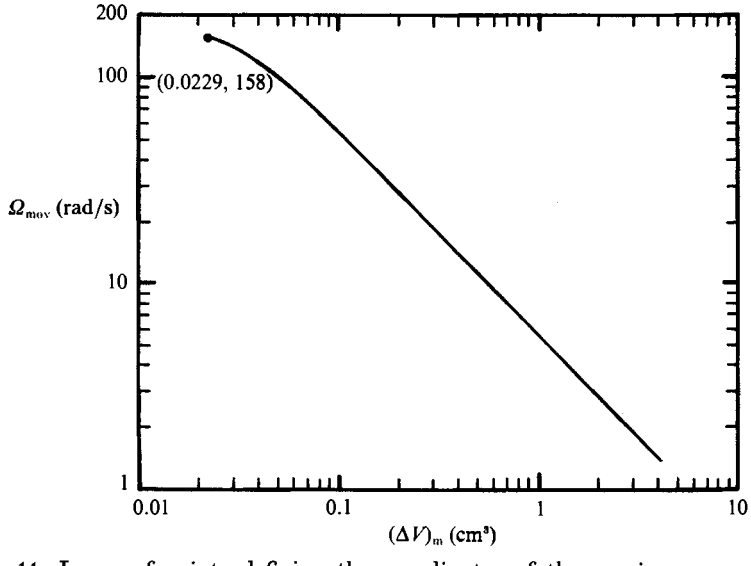

FIGURE 11. Locus of points defining the coordinates of the maximum overfill volume in the $(\Omega_c, \Delta V)$ stability plane computed at the average experimental values $Bo = 1.924$ and $\overline{W} = 0.378$.

and $(\Delta V)_m$ increase linearly with r_1 is just a reflection of the fact that the area under a meridional section has settled down to a constant value and the overfill volume then increases linearly with mean groove radius. For $r_1 \ll 1$ the approximate asymptotic trends are

$$\left.\begin{aligned} (\Delta V)_m &\sim 0.0229 \quad (\text{cm}^3), && (11a)\\ \Omega_{mov} &\sim 158 \quad (\text{rad/s}) && (11b)\\ \frac{(\Delta V)_m}{(\Delta V)_0} &\sim \frac{0.076}{r_1^{0.82}}. && (11c) \end{aligned}\right\} \quad (r_1 \to 0),$$

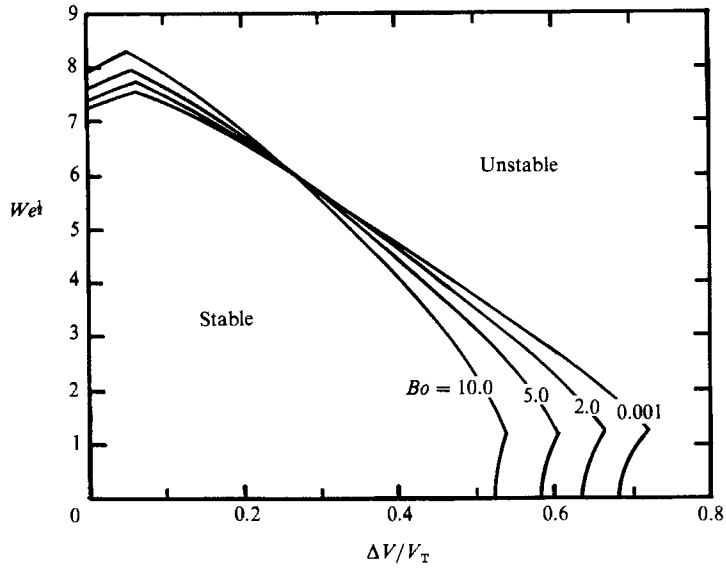

FIGURE 12. Bond-number variation of the composite stability boundary for Track 2 computed for $(\theta_1)_R = 30°$ and $(\theta_{1,2})_A = 165°$.

By virtue of (11a) it is clear that the singularity in (11c) is due to $(\Delta V)_0$ tending to zero algebraically as $r_1 \to 0$. No significance is given to the exponent in (11c) as it is likely to be Bond-number dependent. Plotted meniscus profiles for zero rotation in this limit look very much like scaled-down versions of the $\Omega = 0$ profile in figure 9, i.e. a slow rise in fluid elevation away from the outer rim that peaks near $(r - r_1) = 0.25$ and a more rapid descent to zero amplitude at the inner wall where $(\theta_1) = (\theta_1)_A = 176.5°$. No tendency towards signularity in profile curvature for $r_1 \to 0$ was observed in the numerical solutions. The locus of corner points $(\Omega_{mov}, (\Delta V)_m)$ defining the position of the maximum volume in the regime diagram is plotted in figure 11. Note from (10a) and (10b) that as Ω_{mov} increases from zero, the corner points follow the asymptotic trajectory

$$\Omega_{mov} \sim \frac{5.75}{(\Delta V)_m} \qquad ((\Delta V)_m \to \infty), \tag{12}$$

pass through a short transition, and ultimately terminate at the accumulation point (0.0229 cm^3, 158 rad/s). Consideration of the foregoing results suggests that the inequalities $0 \leqslant \Omega_{mov} \leqslant \Omega_m$ and $0 \leqslant (\Delta V)_0 \leqslant (\Delta V)_m$ hold for all r_1 throughout its semi-infinite range $[0, \infty]$, and it is probable that this result holds true for other Bond numbers as well. It should be noted, however, that the limit $r_1 \to 0$ would not be physically possible for systems with advancing contact angles $\alpha_A > \frac{1}{2}\pi$ for which $(\theta_1)_A > \pi$. In this case the overhanging free-surface profiles at low values of Ω would touch along the axis of symmetry and merge to form a circular liquid pool of radius R_2 before the limit $R_1 = 0$ is reached.

5.2. *Bond number and contact angle hysteresis*

Figure 12 exhibits non-dimensional regime diagrams for Track 2 covering four decades of Bond number computed for $(\theta_{1,2})_A = 165°$ and $(\theta)_R = 30°$. Since there is no perceptible change in plotted results for $Bo < 0.01$, the curve computed for $Bo = 0.001$ may be regarded as the limiting critical zero-Bond-number boundary. Above

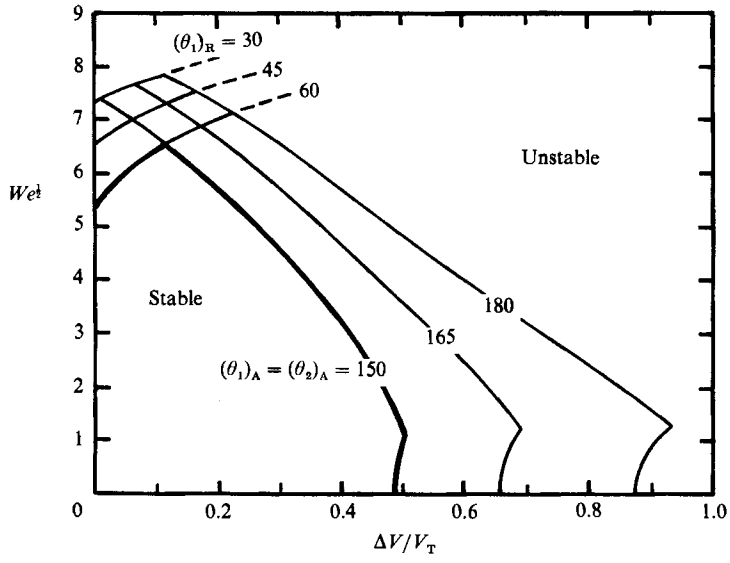

FIGURE 13. Variation of the composite stability boundary computed at $Bo = 1.967$ for Track 2 as a function of the advancing and receding contact angles.

$Bo = 0.1$ noticeable changes take place and contact line movement is suppressed near the lower corner at the maximum overfill volume and enhanced near the upper corner at the maximum Weber number. In terms of the channel dimensions given in table 1, the domain boundaries in figure 12 correspond to experiments performed with water in gravitational fields in the range 0–5g.

The effects of contact angle hysteresis on contact line movement for menisci formed in Track 2 at $Bo = 1.967$ are displayed in figure 13. The advancing and receding contact angles vary over the ranges $30° \leqslant \alpha_R \leqslant 60°$ and $60° \leqslant \alpha_A \leqslant 90°$ corresponding to $30° \leqslant (\theta_1)_R \leqslant 60°$ and $150° \leqslant (\theta_{1,2})_A \leqslant 180°$, respectively. These values have been selected so that in all cases $(\alpha_A - \alpha_R) \geqslant 0$ and hence all nine combinations of the stability branches constitute physically realizable critical static configurations. The innermost boundary marked by the thick line corresponds to zero contact angle hysteresis and encompasses the smallest domain of static states. The finite domain of stable states in this case is due solely to the presence of the corners which allow contact angle movement through the angular range $(\pi - \beta) = \frac{1}{2}\pi$ according to equation (8). As $(\theta_1)_R$ decreases or $(\theta_{1,2})_A$ increases, the domain of stable states increases owing to the corresponding increase in effective contact angle hysteresis. Figure 13 shows that the domain of critical static states is more sensitive to variations in advancing contact angle than receding contact angle.

6. Discussion and conclusion

A numerical study of the shape of pinned annular capillary surfaces overfilling circular grooves of rectangular section formed in a horizontal flat disk undergoing rigid rotation has been presented. Regime diagrams for the existence of static contact lines are determined based on the intrinsic contact angle hysteresis of the system and the contact angle hysteresis induced when liquid is pinned to the corner of a solid boundary. Both qualitative observation and direct measurement suggest that for contact angles $\alpha < 86.5°$, contact line movement is brought about by one of three

mechanisms based on measured advancing and receding contact angles. A contact circle will move when either: (i) $\theta_1 \geqslant (\theta_1)_A$ and liquid advances radially inward across the horizontal plate; (ii) $\theta_2 \geqslant (\theta_2)_A$ and liquid advances radially outward across the horizontal plate; or (iii) $\theta_1 \leqslant (\theta_1)_R$ and liquid recedes vertically downward along the inner wall. The directions of incipient contact line movement brought about by these mechanisms are depicted schematically in figure 4. Experiments reveal that contact line motion along the $(\theta_1)_R$ and $(\theta_2)_A$ domain boundaries accessed via a line of constant overfill volume always produce a spontaneous explosive outward radial spray of liquid from the grooves. Contact line movement along the $(\theta_1)_A$ branch accessed via a line of constant disk rotation rate, on the other hand, always occurred as a relatively gentle radially inward displacement of fluid across the inner rim of the groove of the type referred to as 'slip-stick' movement. These findings are interpreted as follows. An outward displacement of the contact line at the outer rim moves liquid into a region of enhanced centripetal force field with a resulting acceleration of the fluid further outward. Hence this provides a mechanism for hydrodynamic instability of the rotating liquid ring. An inward displacement of the contact line at the inner rim, on the other hand, moves liquid into a region of lower centripetal force field and the fluid displacement is retarded. In this case there appears to be no obvious mechanism for instability.

Although the experimental data follow the trend of the critical static configurations for each groove, it is a bit disconcerting that they do not agree within experimental error. Resonances excited by the small residual motor vibrations conceivably could be responsible for the early onset of instability observed at high disk rotation rates. However, since the power spectra of the external disturbances were not measured and because no analytical results for standing waves on pinned menisci with finite overfill volume are available, a reasonable assessment of possible wave resonance excitation cannot be made. There is also the possibility that the macroscopic advancing and receding contact angles varied across the surface of the plate due, for example, to water absorbed by the anodized surface with time or to variations in surface roughness at the machined corners of each groove as evidenced by the microscopic wrinkling of the liquid surface around its contact circles. A partial check on this possibility was made by an indirect *in situ* measurement of the advancing contact angle at the point of incipient contact line movement in the outermost groove (Track 7) which was within the focal length of our goniometer. With the goniometer focused on the outer edge of the meniscus on a stationary disk, the radially inward movement of the inner contact line was observed when the outer contact angle reached $\theta_2 = 176 \pm 1°$. Numerical solution for the meniscus profile at this outer contact angle then gives $\theta_1 = 176.21 \pm 1°$ for $\Omega = 0$. This agrees remarkably well (perhaps fortuitously) with the measured values $\theta_A = 176.5 \pm 1.5°$ obtained from direct measurement of the advancing contact angle as described in §3.2. It is noted, however, that this does not preclude possible contact angle variability between grooves. Similar measurements for the six inner grooves were not made because the tangency points of their menisci were just out of the focal range of the goniometer.

The limited experiments performed thus far suggest that for static contact angles $\alpha < \frac{1}{2}\pi$, approximately, the stability of axisymmetric menisci pinned to the corners of a circular channel of rectangular section in rigid rotation can be determined by solutions of (5) subject to the restriction on contact angles given by (9). We venture to suggest that solution of (5) and (9) will describe stable menisci for contact angles $\frac{1}{2}\pi < \alpha < \pi$ at least over some range of wavenumbers k. This is based on the

conjecture that the vortex lines set up in the rigidly rotating fluid will be a stabilizing factor. Furthermore, the addition of contact lines to a capillary system enhances stability. In the absence of gravitational and centripetal potential fields, Davis (1980) cites the example of the static liquid cylinder originally studied by Rayleigh (1879). When the cylinder is free of contact lines, stability is certain for wavenumbers $k > 1$. If a thin wire is brought into contact with the liquid cylinder along a generator, thereby forming a single contact line, the region of certain stability is increased to $k > \frac{1}{2}\sqrt{3}$. This stabilization occurs because the addition of the fixed contact line precludes purely axisymmetric perturbations as admissible disturbance modes. The annular meniscus considered here, static in its rotating frame, has two circular contact lines. This is one more than the closed axisymmetric sessile drop, itself stable (in the absence of rotation) for all contact angles $\alpha < \pi$ according to Michael & Williams (1977). The above arguments suggest that at least conditional stability for pinned rotating annular capillary surfaces may be expected over a range of contact angles wider than that explored in the present experiments. Final word, of course, must await a rational stability treatment which properly includes the combined effects of gravitational, centripetal and Coriolis forces in the dynamical equations of motion.

It is noted that the meniscus shapes for the rotating system studied here are not similar to capillary surfaces pinned to the corners of concentric annular grooves embedded in a stationary vertical cone whose central axis is aligned with gravity. This is because the centripetal body force acting throughout the fluid volume is non-uniform: it varies linearly with radius. The analogy only holds in the limit where the ratio of groove width to mean groove radius tends to zero.

An interesting feature found in this study is the existence of a region of static states inaccessible to experiments conducted along a line of constant overfill volume. The region projected above the $(\theta_1)_A$ boundary but below the $(\theta_2)_A$ boundary defines this unique domain in the $(\Omega_c, \Delta V)$ regime diagram, the static states of which are accessible only by adding liquid to a rotating groove. The maximum overfill volume of the system occurs at the extremity of this region, at the intersection of the $(\theta_1)_A$ and $(\theta_2)_A$ domain boundaries. Numerical studies indicate that gravitational effects only become important when $Bo > 0.1$, approximately. The numerical studies also show that the domain of contact line stability may be significantly enhanced either by decreasing the inner radius at fixed groove width or by increasing the contact angle hysteresis of the system.

We very much appreciate the assistance of machinist Karl Rupp and electronics engineer Rich Cowgill at the University of Colorado for their work in constructing the rotating table and drive system. Marathon Oil Company in Denver aided in our initial efforts to make precise contact angle measurements. We appreciate receiving the goniometer base as a donation to our fluids laboratory from Melles Griot Corporation. Drs K. Kirkkopru, J. Padday and D. Needham shared in useful discussions on the subject of this research. Extensive and constructive comments by two referees did much to clarify and enhance the presentation of this report. One of the authors (P.D.W.) is particularly grateful to the Science and Engineering Research Council for a Visiting Fellowship during the final stages of manuscript preparation. P.D.W. also acknowledges the gracious hospitality of the School of Mathematics at the University of East Anglia and especially that of his host and colleague Professor N. Riley.

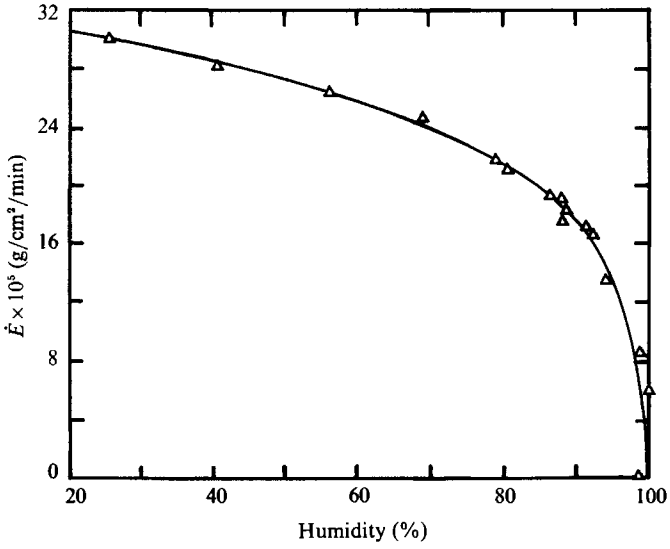

FIGURE 14. Evaporation rate of HGLC grade water as a function of relative humidity measured at 68 ± 1 °F.

Appendix. Sources of error

In order to minimize water evaporation during an experiment, the rotating table was housed in a room constructed to regulate temperature and humidity. The control chamber was equipped with a thermostatically controlled quartz heater, an ultrasonic humidifier, a fan, a thermometer and a relative humidity gauge. The evaporation rate of HPLC grade water at fixed humidity was measured by monitoring the weight loss of a water sample in a cylindrical plastic container with free-surface area 18.47 cm^2. At each humidity setting the weight loss at 68 °F over a period of approximately one hour was measured with a Mettler PC 180 electronic balance accurate to 0.001 g. The measured rates of evaporation $\dot{E}$ as a function of relative humidity are plotted in figure 14. The results give rates of evaporation in the range 16–20 g/cm^2/min for the experimental conditions listed in table 1. To assess whether this contributed to any significant measurement error we consider how the experiment was conducted for two tracks, one of small and the other of large mean radius. The greatest weight loss in either case must occur at the largest overfill volume, which exposes the greatest free-surface area to the surrounding air and takes the longest time to fill. Figure 7 shows that the largest overfill volumes for this experiment are bounded by the overfill volume of a half-torus with outer diameter R_2 and inner diameter R_1. Therefore, half the surface area of a torus, $\pi^2 \bar{R} W$, will be employed in the following calculations since it represents an upper bound on the area of the evaporating capillary surface. Here $\bar{R}$ is the average radius of a track. Track 1 was filled with a single 5 ml pipette in about one minute and three additional minutes were taken to cover the plate, accelerate the disk to near-critical, wait 30 s for the fluid to come to solid-body rotation and slowly increase the speed to the observed point of contact line movement. From table 1 an upper bound on the surface area of 3.83 cm^2 is calculated and, using $\dot{E} = 0.0002$ g/cm^2/min, a weight loss of 0.0031 g in four minutes is found. This represents a water volume of 0.0031 cm^3 corresponding to roughly $\frac{2}{5}$ the diameter of the plotting symbol for measurements presented in figure 8(*a*) performed in Track 1. For Track 6 two pipettes sometimes

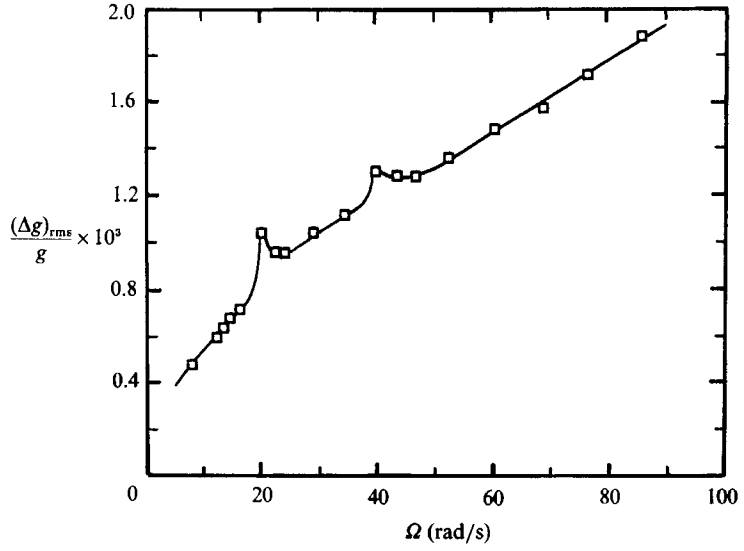

FIGURE 15. Normalized r.m.s. g-jitter of the experimental platform due to residual motor vibrations transmitted through the belt-and-pulley system measured as a function of disk angular frequency.

were used to fill the groove – the 10 ml pipette served to rapidly fill the groove volume V_0 and the 5 ml pipette was used to add the overfill volume ΔV. In this case the experiment could take as long as six minutes and calculations then give a maximum water volume loss of 0.050 cm^3 which corresponds to roughly $\frac{3}{5}$ the diameter of a plotting symbol for the measurements given in figure 8(f). Thus errors in volume measurement due to evaporation are negligible for the time periods used to perform these experiments. The precision with which the pipettes could be read is also small relative to plotting symbol diameters and hence experiments conducted with a preset volume (open circles in figure 8) have no horizontal error bars. The vertical error bars attached to the open circles indicate the scatter in repeatability of the measured critical frequency for experiments conducted under nearly identical conditions. Similarly, for experiments performed at a preset rotation rate (closed circles in figures 7 and 8), frequency measurement errors fall within the diameter of the plotting symbols and horizontal error bars here indicate the scatter in repeatability of critical overfill volumes at which contact line movement was observed.

A source of experimental error whose effect on the stability measurements is difficult to ascertain is the g-jitter induced by vibrations of the stepper motor and drive system. The r.m.s. magnitude of the acceleration jitter on the frame supporting the rotating disk, denoted $(\Delta g)_{\rm rms}$, was measured with a sensitive commercial accelerometer having calibration constant 0.4 V/g, where g is Earth's gravity. Little difference was found between measured vertical and horizontal r.m.s. accelerations, indicating a rather isotropic g-jitter field. The measured values of $(\Delta g)_{\rm rms}/g$ as a function of plate frequency are presented in figure 15. Two small resonant peaks at $\Omega \approx 20$ and 40 rad/s are apparent, but otherwise the induced jitter increases monotonically with disk frequency. Although the maximum induced r.m.s. jitter is only 0.2% g, its influence on the stability measurements is not easy to assess in the absence of a detailed study of fluid resonance in an overfilled channel with the liquid pinned to its corners.

REFERENCES

BENJAMIN, T. B. 1980 Theoretical problems posed by gravity–capillary waves with edge constraints. In *Trends in Applications of Pure Mathematics to Mechanics, III* (ed. H. Zorski), pp. 40–58. Pitman.

BENJAMIN, T. B. & GRAHAM-EAGLE, J. 1985 Long gravity–capillary waves with edge constraints. *IMA J. Appl. Maths* **35**, 91.

BENJAMIN, T. B. & SCOTT, J. C. 1979 Gravity–capillary waves with edge constraints. *J. Fluid Mech.* **92**, 241.

COGHILL, W. H. & ANDERSON, C. O. 1923 Bureau of Mines, Tech. Paper 262.

CONCUS, P. 1968 Static menisci in a vertical right circular cylinder. *J. Fluid Mech.* **34**, 481.

DAVIS, S. H. 1980 Moving contact lines and rivulet instabilities. Part 1. The static rivulet. *J. Fluid Mech.* **98**, 225.

DETTRE, R. H. & JOHNSON, R. E. 1965 Contact angle hysteresis. IV Contact angle measurements on heterogeneous surfaces. *J. Phys. Chem.* **69**, 1507.

DUSSAN V., E. B. 1979 On the spreading of liquids on solid surfaces: Static and dynamic contact lines. *Ann. Rev. Fluid Mech.* **11**, 371.

DUSSAN V., E. B. 1985 On the ability of drops or bubbles to stick to non-horizontal surfaces of solids. Part 2. Small drops or bubbles having contact angles of arbitrary size. *J. Fluid Mech.* **151**, 1.

FINN, R. 1986 *Equilibrium Capillary Surfaces.* Springer.

GOODWIN, R., RICE, D. & MIDDLEMAN, S. 1988 A model for the onset of motion of a sessile liquid drop on a rotating disk. *J. Colloid Interface Sci.* **125**, 162.

HECKERMAN, D., GARRETT, S., WILLIAMS, G. A. & WEIDMAN, P. D. 1979 Surface tension restoring forces on gravity waves in narrow channels. *Phys. Fluids* **22**, 2270.

HUH, C. & SCRIVEN, L. E. 1969 Shapes of axisymmetric fluid interfaces of unbounded extent. *J. Colloid Interface Sci.* **30**, 323.

KITCHENER, J. A. 1964 Foams and free liquid films. In *Recent Progress in Surface Science*, vol. 1, p. 51. Academic.

MICHAEL, D. H. & WILLIAMS, P. G. 1977 The equilibrium and stability of sessile drops. *Proc. R. Soc. Lond.* A **354**, 127.

PADDAY, J. F. 1971 The profiles of axially symmetric menisci. *Phil. Trans. R. Soc. Lond.* A **269**, 265.

PADDAY, J. F. & PITT, A. R. 1973 The stability of axisymmetric menisci. *Phil. Trans. R. Soc. Lond.* A **275**, 489.

PRINCEN, H. M. & MASON, S. G. 1965 Shape of a fluid drop at the fluid-liquid interface. II. Theory for three-phase systems. *J. Colloid Sci.* **20**, 246.

RAYLEIGH, LORD 1879 On the instability of jets. *Proc. Lond. Math. Soc.* **10**, 4.

SCOTT, J. C. 1979 The preparation of clean water surfaces for fluid mechanics. In *Surface Contamination: Genesis, Detection and Control*, vol. 1 (ed. K. L. Mittal), p. 447. Plenum.

SCOTT, J. C. 1981 The propagation of capillary–gravity waves on a clean water surface. *J. Fluid Mech.* **108**, 127.

SCOTT, J. C. & BENJAMIN, T. B. 1978 Waves in narrow channels: faster capillary waves. *Nature* **276**, 803.

WEIDMAN, P. D. & NORRIS, J. A. 1987 Capillary gravity waves with fixed contact lines: An approximate analysis. *Physicochem. Hydrodyn.* **9**, 393.